

Solid-state additive manufacturing of porous Ti-6Al-4V by supersonic impact

Atieh Moridi^{a,b,c,*}, Elizabeth J. Stewart^{a,d}, Akane Wakai^b, Hamid Assadi^e, Frank Gartner^f, Mario Guagliano^c, Thomas Klassen^f, Ming Dao^{a,*}

^a Department of Materials Science and Engineering, Massachusetts Institute of Technology, Cambridge, MA 02139, USA

^b Sibley School of Mechanical and Aerospace Engineering, Cornell University, Ithaca, NY 14853, USA

^c Department of Mechanical Engineering, Polytechnic University of Milan, Milan, Italy

^d Department of Chemical Engineering, Worcester Polytechnic Institute, Worcester, MA 01609, USA

^e Brunel University London, Brunel Centre for Advanced Solidification Technology (BCAST), Uxbridge, United Kingdom

^f Helmut Schmidt University, University of the Federal Armed Forces, Hamburg, Germany

ARTICLE INFO

Article history:

Received 23 July 2020

Revised 12 October 2020

Accepted 19 October 2020

Keywords:

Cold spray

Additive manufacturing

Cellular structure

Titanium alloy

Biocompatible

ABSTRACT

Additive manufacturing of functional metallic parts based on layer-by-layer melting and solidification suffers from the detrimental effects of high-temperature processing such as large residual stresses, poor mechanical properties, unwanted phase transformations, and part distortion. Here we utilize the kinetic energy of powder particles to form a solid-state bonding and overcome the challenges associated with the high temperature processing of metals. Specifically, we accelerated powders to supersonic impact velocities (~600 m/s) and exploited plastic deformation and softening due to high strain rate dynamic loading to 3D print Ti-6Al-4V powders at temperatures (800 °C, 900 °C) well below their melting point (1626 °C). By using processing conditions below the critical powder impact velocity and controlling the surface temperature, we created mechanically robust, porous metallic deposits with spatially controlled porosity (apparent modulus 51.7 ± 3.2 GPa, apparent compressive yield strength 535 ± 35 MPa, porosity $30 \pm 2\%$). When the mechanical properties of solid-state 3D printed Ti-6Al-4V were compared to those fabricated by other additive manufacturing techniques, the compressive yield strength was up to 42% higher. Post heat treatment of solid-state printed porous Ti-6Al-4V modified the mechanical behavior of the deposit under compressive loading. Additionally, the 3D printed porous Ti-6Al-4V was shown to be biocompatible with MC3T3-E1 SC4 murine preosteoblast cells, indicating the potential biomedical applications of these materials. Our study demonstrates a single-step, solid-state additive manufacturing method for producing biocompatible porous metal parts with higher strength than conventional high temperature additive manufacturing techniques.

© 2020 Elsevier Ltd. All rights reserved.

1. Introduction

Conventional processing routes to fabricate metallic cellular structures constrain material selection [1–3] and part geometry, which is mostly limited to planar shapes [4,5]. Additionally, powder metallurgy based methods for creating cellular solids restrict the pore size and shape while requiring post processing steps to remove sacrificial space holders (i.e. by dissolution or thermal degradation) [2]. The need for specific mechanical and functional properties as well as manufacturing flexibility for a wide range of metallic materials has brought interest in using additive manufac-

turing techniques in various industrial applications [6–10]. Additive manufacturing is promising for fabricating complex geometries but has several drawbacks associated with the high temperature processing of metals that often result in undesired mechanical properties [8,11–14].

Supersonic powder deposition (cold spraying) is a technology that is used to overcome the challenges associated with the high temperature processing of metallic parts [15]. In cold spray deposition, plastic deformation due to a high strain rate dynamic loading is utilized to form solid-state bonding between metallic powders [16] – the building blocks of the final parts. In cold spraying, powders are accelerated by a supersonic jet of compressed gas through a de Laval nozzle [15]. This is unlike other additive manufacturing processes where powders are either laid down on a powder bed as is done in selective laser melting (SLM) and selective electron

* Corresponding authors.

E-mail addresses: moridi@cornell.edu (A. Moridi), mingdao@mit.edu (M. Dao).

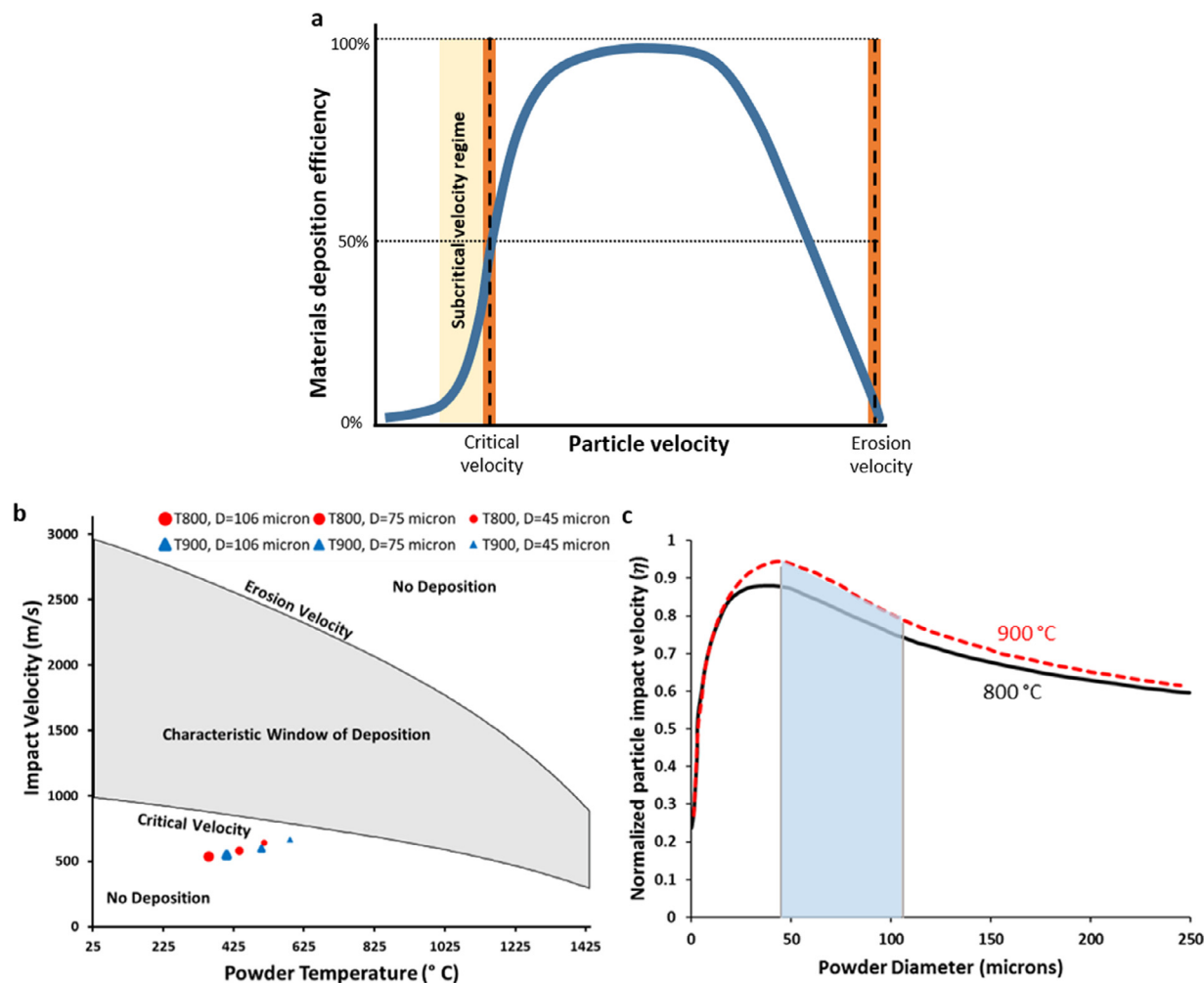


Fig. 1. Supersonic powder deposition and determination of deposition parameters. (a) Schematic of materials deposition efficiency as a function of particle velocity. Typically, parts are printed using process parameters that result in a particle velocity that lies between the critical velocity and erosion velocity. However, prints were produced within the subcritical range (shaded in yellow) to induce porosity in this study. (b) Calculated impact conditions for parameter sets used to manufacture porous deposits with carrier gas temperature $T = 800$ °C (red circles) and $T = 900$ °C (blue triangles) at $P_{gas} = 40$ bars. Symbol size is indicative of particle size, and thresholds for deposit formation in terms of critical velocity. The powder impact conditions are intentionally outside of the calculated window of deposition used to print porous metallic deposits. (c) Normalized particle impact velocity (η) as a function of particle diameter with the powder size distribution used in our experiments (45–105 μm) shaded in blue. (For interpretation of the references to colour in this figure legend, the reader is referred to the web version of this article.)

beam melting (SEBM) [17,18] or fed by a powder feeder at velocities up to 10 mm/s as is done in directed energy deposition (DED) [19–21]. Some Ti-6Al-4V porous structures have been fabricated by additive techniques such as SLM [22], SEBM [23–25], DED [26], and binder jet [27]. These studies have produced porous geometries by using a pattern of holes that occupies a certain percentage of the build volume or by printing a scaffold structure (a toolpath-based porosity). These porous parts have porosities ranging between 18% and 80% [22–27]. To the authors' best knowledge, designing porous structures has never been studied using cold spray, and the high deposition rate of cold spray makes it a more efficient method of fabrication than the methods highlighted above.

In cold spray, the powder impact velocity can be tuned to control the adhesion of metal powders, as shown schematically in Fig. 1(a) [15,28]. There are two important particle velocities: the critical impact velocity (v_{cr}) and the erosion velocity (v_{er}). The critical impact velocity is the particle velocity at which the deposition efficiency (the proportion of particles that adhere to the substrate or previous layer compared to the overall powder particles delivered from the nozzle) is 50% [16]. As the particle velocity increases, deposition efficiency also increases until it reaches saturation where the optimum coating conditions are met in a typical

full density print. Beyond the saturation limit, the deposition efficiency decreases with an increase in particle velocity due to hydrodynamic penetration of the substrate by particles. Eventually, increases in particle velocity result in the erosion velocity, where the kinetic energy of the particles becomes too large for the successful adhesion of powders to the substrate and the deposition efficiency becomes 0%. If the powder impact velocity (v_i) exceeds the critical impact velocity and stays below the erosion velocity, the majority of the powder will adhere to the surface and form a dense deposit [16,29]. The critical and erosion velocities are temperature-dependent and define the characteristic window of deposition on the velocity-temperature plane. In the present work, we intentionally worked in the subcritical velocity domain—a domain that has been avoided so far—to create porous metal deposits from Ti-6Al-4V alloy powders in a single step. The subcritical velocity domain is where the normalized particle impact velocity ($\eta = \frac{v_i}{v_{cr}}$) is smaller than 1. The nozzle traverse speed was tuned to create uniform porosity throughout the thickness of the deposit. Deposits were analyzed with respect to porosity, surface roughness, liquid contact angle on substrate surface, and mechanical behavior. Moreover, the potential of post heat treatment to tune the mechanical properties of the porous deposits was demonstrated. Finally, these

deposits were shown to support cell growth, which reveals that this method could be used to fabricate materials for biomedical implants and devices.

2. Materials and methods

2.1. Materials

Ti-6Al-4V alloy powders (Advanced Powders and Coatings, Boisbriand, Canada) with a Gaussian size distribution and particle sizes between 45 and 106 μm were used in this study. The powders were printed on commercially pure Ti plates of 3-mm thickness.

2.2. Supersonic particle deposition

Supersonic particle deposition was performed using a CGT-Kinetic® 8000 high-pressure cold spray system. Titanium substrates were used as support structures. The key deposition parameters are process gas pressure, process gas temperature, and nozzle scan velocity. We studied four different deposition procedures by varying traverse speed and gas temperature. Specifically, slow (6 m/min) and fast (12 m/min) nozzle traverse speeds at two different preheated carrier gas temperatures (800 and 900 °C) were examined. Carrier gas pressure (40 bar), carrier gas (Nitrogen) and number of passes (5) were kept constant.

2.3. Subcritical deposition

To determine the experimental parameters for subcritical deposition, fluid dynamics calculations (finite volume two-phase flow analysis of gas and powder in the nozzle and in the free jet) available in a commercially available software from kinetic-spray-solutions (KSS GmbH, Buchholz, Germany) were used [28,30]. These model-based calculations were validated through comparisons with particle velocities measured using Laser Doppler Anemometry (LDA) [31]. The calibration calculations and the measured velocities are plotted in Supplemental Fig. S1. The comparison shows good agreement between the calibration calculations and the velocities obtained by the LDA. These verification experiments have also been used as a basis for introducing correction functions into the officially released version of KSS software (used in this study) so that calculations closely match experimentally observed values.

The contour plot of the normalized particle impact velocity (η) as a function of gas pressure and temperature was used as a guideline to choose the experimental processing parameters. We kept the pressure constant at the maximum operating pressure of the device ($P = 40$ bar) and chose gas temperatures to tune for η values close to but smaller than 1 to deposit in the subcritical domain. In several iterations, the gas temperatures fulfilling this requirement for the selected powder sizes were determined to range between 800 and 900 °C. Powder sizes were selected to deviate from the optimum and be larger to allow for a better adjustment of the subcritical impact conditions. Using these deposition parameters ($P = 40$ bar and $T = 800$ and 900 °C) and CFD calculations, we calculated the particle velocity and temperature upon impact for three different particle diameters as shown in Fig. 1(b) (45, 75 and 106 μm corresponding to the minimum, median, and maximum diameters in the particle size distribution range). For simplicity, we refer to these deposition conditions as T800 and T900 in this paper, which correspond to the temperatures of the carrier gas. We also calculated the window of deposition for Ti-6Al-4V powders using the respective bulk material properties for the powder size regime used. During the experiments, substrates were preheated by scanning the substrates with the hot carrier gas (800 and 900 °C) for two consecutive passes to promote bonding at

the interface. As a result, a stable growth of porous layers was achieved.

2.4. Porosity and pore size measurements

The porosity of the deposits before and after the heat treatment was determined by quantitative image analysis of the polished cross sections. The as-printed samples were prepared by mechanical polishing using several SiC sandpapers and diamond suspensions up to 1 μm , followed by 0.5 hour of polishing using a SiO₂ colloidal suspension. Binary images of the polished cross sections at the same magnification were used to calculate the ratio of pore (black voids) to the total surface area. The average and standard deviation of five measurements in different areas are reported. The porosity values reported in this study are a slight overestimate as some particles were lost during the grinding and polishing process, which is not accounted for in the image analysis. Although the bonding between the impacted particles is strong enough for particles to attach to one another, they only adhere in certain areas. Depending on the direction of the cut and the local porosity structure, these bonded areas may already have been eliminated, so parts of a particle may fall out during polishing. In addition, we cannot completely exclude that there are some weakly bonded particles lodged within the layers. These powder particles may have come loose during the polishing process. Therefore, the density of 3D printed samples was also measured using the Archimedes principle, and the density ratio was corroborated with the image analysis results. The porosities were determined with the aid of density calculation and hydrostatic weighing. The theoretical density of Ti used for this determination was 4.5 g/cm³. For each specimen, measurements were repeated three times, and the mean value is reported.

2.5. Deposit powder size distribution

To understand the mechanism of the porous structure formation, we analyzed the powder size distribution in the deposits. The diameter of the adhered powders in 3D printed porous Ti-6Al-4V ($T = 800$ °C) was determined by measuring the particle size in ImageJ. Three SEM images were taken at 150X and the diameters of 100 particles per image were measured (a total of 300 powder particles across the three images).

2.6. Compression testing

Quasi-static uniaxial compression tests were conducted on Gatan MTEST2000 Uniaxial Testing Stage. The samples were cut into cross sections of 2 cm \times 2 cm, and the specimens were loaded parallel to their build direction. Three samples were tested for each condition. The average and the standard deviation of the stress-strain behavior were determined.

2.7. Heat treatment

Ti-6Al-4V is a two-phase alloy composed of both α and β phases at room temperature. The α -to- β phase transformation (β -transus temperature) occurs at ~ 970 °C [32]. Heat treatments above (1050 °C) and below (840 °C) the β -transus temperature were performed in a tube furnace purged with Argon and at a heating rate of 10 °C/min. The specimens were maintained at the designated temperature for 2 hours followed by furnace cooling.

2.8. X-ray Diffraction

X ray diffraction (XRD) analyses were performed using CuK α radiation on a PANalytical X'Pert Pro diffraction instrument operating

Table 1
Constant values for calculating contact temperature at impact zone according to Eq. (1) [35,36].

Constants		
C (J/Kg·K)	Specific heat	526
β	Deformation localization	0.1
K (W/mK)	Conductivity	7.2
ρ (Kg/m ³)	Density	4430
T_c^0 (K)	Initial contact temperature	300
T_{melt} (K)	Melting temperature	1900
H_p (MPa)	Powder hardness	3423
Definitions		
t_c (s)	Contact time	$t_c = \frac{2\varepsilon_p d_p}{v}$
ε_p	Plastic strain	$\varepsilon_p = \exp(-0.6 \frac{H_p}{\rho_p v_p^2})$
h_p	Particle height after impact	
α (m ² /s)	Thermal diffusivity	$\alpha = \frac{k}{\rho c}$
τ	Relative time	$\tau = \frac{t}{t_c}$

at 45 kV and 40 mA between 30 and 60 deg (2θ) at a step size of 0.01 degrees and a counting time of 40 seconds per step.

2.9. Roughness

The InfiniteFocus (Alicona, Austria), an optical device for 3D surface measurements, was used to trace the surface profiles of as-received bulk material and 3D printed specimens using cold spray deposition. The operating principle of the device combines the small depth of focus with vertical scanning to provide topographical information from the variation of focus. The captured information from a 5×5 cm² scanned area was reconstructed into a 3D topographical data set to obtain the following surface roughness parameters: arithmetic average (S_a), root mean square (S_q), maximum valley depth (S_v), and maximum peak height (S_v) [33].

2.10. Calculating contact temperature

The temperature at the impact zone was computed by calculating the temperature rise due to heat released during impact. It was assumed that almost all kinetic energy is converted to heat and that the heat is released in a fraction of particle height (βh_p), where β is the deformation localization coefficient, and h_p is the particle height after impact. This may be taken as a representative estimate for the actual temperature for a relative comparison of the results for different impact parameters. The increase of the contact temperature (T_c) due to heat release during the impact at the contact plane, in the one-dimensional approximation, was calculated as follows [34,35]:

$$T_c(t) = \frac{V_p^3 t_c}{8c\beta\varepsilon_p d_p} \int_0^1 \operatorname{erf}\left(\frac{d_p \beta (1 - \varepsilon_p)}{\sqrt{4\alpha t_c (1 - \tau)}}\right) d\tau \quad (1)$$

where v_p is the powder impact velocity, c is coefficient of specific heat, d_p is particle diameter, ε_p is plastic strain, α is thermal diffusivity, t_c is contact time, and $\tau = \frac{t}{t_c}$ is the relative time. The specific values for constants are tabulated in Table 1.

Dimensional analysis shows that the plastic strain variation during supersonic impact is dependent on the dimensionless parameter $\frac{H_p}{\rho_p v_p^2}$. The expression relating plastic strain to this dimensionless parameter ($\varepsilon_p = \exp\left(C \frac{H_p}{\rho_p v_p^2}\right)$) has the correct asymptotic values i.e. plastic strain approaches 1 as impact velocity goes to infinity, and plastic strain approaches 0 as particle impact velocity approaches 0 [35]. The constant C for the analytical expression was calculated based on a series of finite element simulations at different impact velocities (600 to 1000 m/s in 100 m/s increments) as described in the next section, which turns out to equal 0.6.

Table 2
Ti-6Al-4V properties for finite element simulation [36].

Elastic	Elastic Modulus	E (GPa)	113.8
	Poisson ratio	ν	0.342
Plastic	Johnson Cook constants	A (MPa)	782.7
		B (MPa)	498.4
		n	0.28
		c	0.028
		m	1
	Reference temperature	T_0 (K)	300
	Reference plastic strain rate	$\dot{\varepsilon}_{p0}$	1×10^5

2.11. Finite element model

For calculating the contact temperature, the value of plastic strain in powders during impact is required (according to Eq. 1). An axisymmetric dynamic explicit model was created in ABAQUS 6.14 to determine the plastic strain. The impact of a single Ti-6Al-4V particle ($D = 50 \mu\text{m}$) with rigid substrates was modeled. The Johnson-Cook constitutive equation (Eq. 2), which accounts for strain hardening, strain rate hardening, and thermal softening, describes the powder deformation behavior.

$$\sigma = [A + B\varepsilon_p^n] \left[1 + c \ln\left(\frac{\dot{\varepsilon}_p}{\dot{\varepsilon}_{p0}}\right) \right] \left[1 - \left(\frac{T - T_0}{T_m - T_0}\right)^m \right] \quad (2)$$

where A , B , n , c and m are material constants and are measured by experiments, ε_p and $\dot{\varepsilon}_p$ are the equivalent plastic strain and equivalent plastic deformation rates, and T_0 is the reference temperature. Values for constants are reported in Table 2.

2.12. Cell line and culture methods

Pre-osteoblast MC3T3-E1 Subclone 4 cells of passage number less than P7 were grown in standard culture conditions (37 °C, 5% CO₂) using Alpha Minimum Essential Medium (Life Technologies, Grand Island, NY) supplemented with 10% fetal bovine serum, 1% penicillin, and 1% streptomycin. After trypsinization, 10,000 cells/cm² were seeded and cultured on titanium support materials and porous Ti-6Al-4V for seven days in 12-well tissue culture dishes. Growth media was exchanged every 2–3 days. Four replicates were performed on each substrate to assess the biocompatibility and integration of cells into porous substrates. Biocompatibility and integration of cells into the porous Ti-6Al-4V was inspected using confocal laser scanning microscopy and scanning electron microscopy.

2.13. Imaging and image analysis for biocompatibility studies

For confocal laser scanning microscopy experiments, cells were stained with 2 μM Calcein AM, and 4 μM Ethidium Homodimer-1 from the LIVE/DEAD Viability/Cytotoxicity Kit, for mammalian cells (Molecular Probes, Eugene, OR). Nuclei were labeled using one to two drops/mL NucBlue Live Cell Stain ReadyProbes reagent (Molecular Probes, Eugene, OR). 3D image volumes of cells were obtained using a Nikon A1 Confocal Laser Scanning Microscope (Nikon, Melville, NY) using a 4x, NA 0.2 objective, and a 20x, NA 0.75 objective. Four image volumes were captured at each magnification for each sample. Representative LIVE/DEAD images were presented for each growth condition. The depth that cells grew into the porous deposit was determined by imaging from the coverslip into the sample until stained cells could no longer be observed with the 4x objective. The depth was then computed by multiplying the z-step size (13 μm) by the number of slices into the sample where cells were observed; the average depth and standard error of the mean are reported. Fluorescence images were

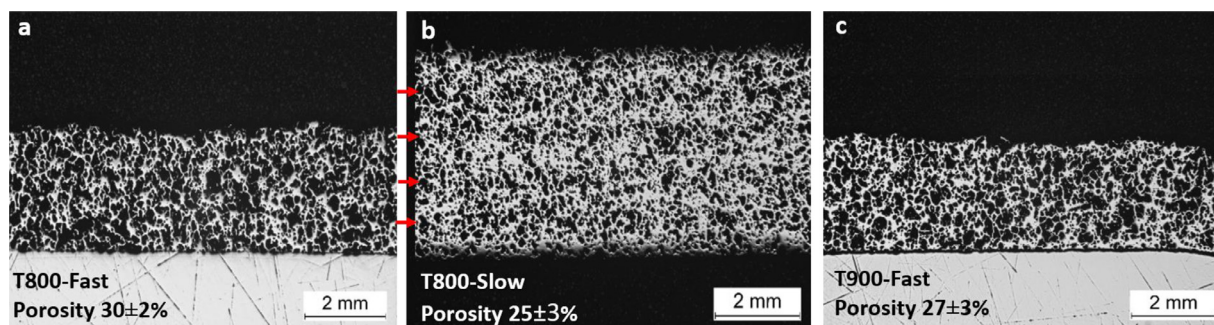


Fig. 2. Optical micrograph of cross sections of materials printed using (a) fast deposition, and (b) slow deposition (the red arrows on the left side of panel b show the interfaces between different passes). (c) Cross section optical micrograph of fast deposition at carrier gas temperature $T = 900$ °C showing similar structure to fast deposition at carrier gas temperature $T = 800$ °C but with less porosity (porosity $27 \pm 3\%$). (For interpretation of the references to colour in this figure legend, the reader is referred to the web version of this article.)

also shown to demonstrate how cells were growing on and between the metal powders that create the porous deposit.

Scanning electron microscopy (SEM) was performed to determine the morphology of the cells on and within the porous Ti-6Al-4V. To prepare the samples for SEM, cells grown on the Ti-6Al-4V porous structure were first fixed in 2.5% glutaraldehyde for one hour, followed by post fixation in 1% osmium tetroxide for one hour. This procedure was followed by ethanol dehydration, where cells were treated with increasing concentrations of ethanol (30%, 50% 70% 90% and 100%) for 15 minutes each.

3. Results and discussion

To ensure that the deposition parameters for our 3D printed deposits remain below the window of deposition, we created and referred to an experimental parameter selection map by performing fluid dynamics calculations as described in Section 2.3. As shown in Fig. 1(b), critical and erosion velocities drop when the powder temperature increases. In addition, all the processing conditions for the powder under investigation lie beneath the characteristic window of deposition. Fig. 1(c) shows the normalized particle impact velocity, η , as a function of powder diameter, which illustrates that a smaller particle diameter results in a higher impact velocity for the range of interest (shaded in blue). Additionally, the plot shows that a higher temperature is associated with higher values for η .

Deposition using a nozzle traverse speed of 12 m/min (fast deposition) with a carrier gas temperature of 800 °C (η between 0.74 and 0.87) corresponds to a deposited thickness-per-path ratio of 0.5 mm and results in $30 \pm 2\%$ porosity with a uniform distribution across the thickness as illustrated in Fig. 2(a). We studied the effect of nozzle traverse speed on deposition kinetics by reducing the nozzle traverse speed to half (6 m/min), which corresponds to a deposited thickness-per-pass ratio of 1 mm (slow deposition). Slow deposition resulted in deposits with $25 \pm 3\%$ porosity. A representative cross section of deposits fabricated with slow deposition is shown in Fig. 2(b). Comparing Fig. 2(a) and (b) shows that slowing the nozzle traverse speed decreases porosity. Decreasing the nozzle traverse speed increases the local surface temperature of the pre-deposited material due to a longer gas-deposit interaction, which enhances the deposit quality [37]. This surface temperature effect on porosity is further confirmed by repeating the fast deposition experiment at a higher temperature (900 °C). When fast deposition was performed with a carrier gas temperature of 900 °C, materials were fabricated with buildup thickness-per-pass similar to fast deposition with a carrier gas temperature of 800 °C but with lower porosities ($27 \pm 3\%$, Fig. 2(c)). Therefore, a variation in deposit surface temperature due to differences in nozzle traverse speed can cause modifications in the mesostructure at the interface between each deposition pass (showing uniform porosity for

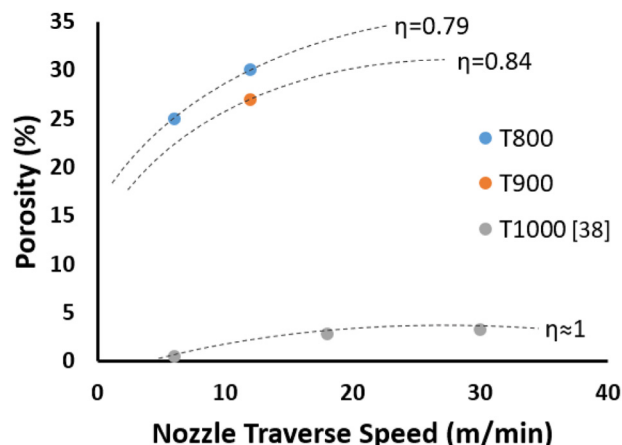


Fig. 3. Porosity vs nozzle traverse speed showing the relationship between porosity, normalized particle impact velocity (η), and nozzle traverse speed (V_N) for T800, T900, and T1000 [38]. The logarithmic relationship between V_N and porosity is shown along with increasing porosity with decreasing η .

fast depositions and dense-porous layered structure for slow depositions). The results show that the porosity of the deposit (ρ) can be controlled by η and nozzle traverse speed ($\rho = f(V_N, \eta)$). η is a function of the deposition parameters (i.e. gas pressure, temperature, powder diameter). Deposition parameters are summarized in Table 3. Porosity is plotted against the nozzle traverse speed in Fig. 3 along with those of Ti-6Al-4V cold sprayed samples printed at $\eta \approx 1$ [38]. The relationship between porosity and nozzle traverse speed is known to be logarithmic, where porosity increases as V_N increases and as η decreases [38]. Porosity measurement using Archimedes principal is also reported in the table, which shows slightly lower values with respect to the image analysis results. Results discussed beyond this point are those of printed deposits with $30 \pm 2\%$ porosity (fast deposition with 800 °C carrier gas temperature) unless noted otherwise.

High velocity impact during cold spray deposition can cause inhomogeneous deformation and localized heating of the interacting surfaces. To study the possible influences of particle sizes, the contact temperature was analyzed by the temperature rise at the impact zone as described in Section 2.10. Fig. 4(a) shows a plot of powder temperature at the contact plane versus impact velocity for different powder diameters from 5 μm to 100 μm at the end of contact ($t = t_c$). Velocities used in the present experimental work ranged from 580 m/s to 700 m/s considering the heterogeneity of the powder sizes, as depicted by the shaded area. As shown in Fig. 4(a), the contact temperatures for different powder sizes were found to lie below the material's melting point

Table 3

Experimental conditions used for cold spray deposition of titanium powders. Process gas pressure (40 bar), process gas (nitrogen) and number of passes (5) were kept constant, while temperature and scan velocity were varied. Porosity from image analysis and Archimedes' principle are reported in the last two columns, respectively. The processing parameters from [38] are also presented.

Group name	Process gas temperature (°C)	Scan velocity (m/min)	η for $D = 75 \mu\text{m}$	Porosity (Optical method)	Porosity (Archimedes principle)	Reference
T800-slow	800	6	0.79	$25 \pm 3\%$	$22 \pm 0.07\%$	Current study
T800-fast	800	12	0.79	$30 \pm 2\%$	$27 \pm 0.1\%$	
T900-fast	900	12	0.84	$27 \pm 3\%$	$24 \pm 0.08\%$	[38]
T1000	1000	6	~1	0.5%	-	
T1000	1000	18	~1	2.7%	-	
T1000	1000	30	~1	3.2%	-	

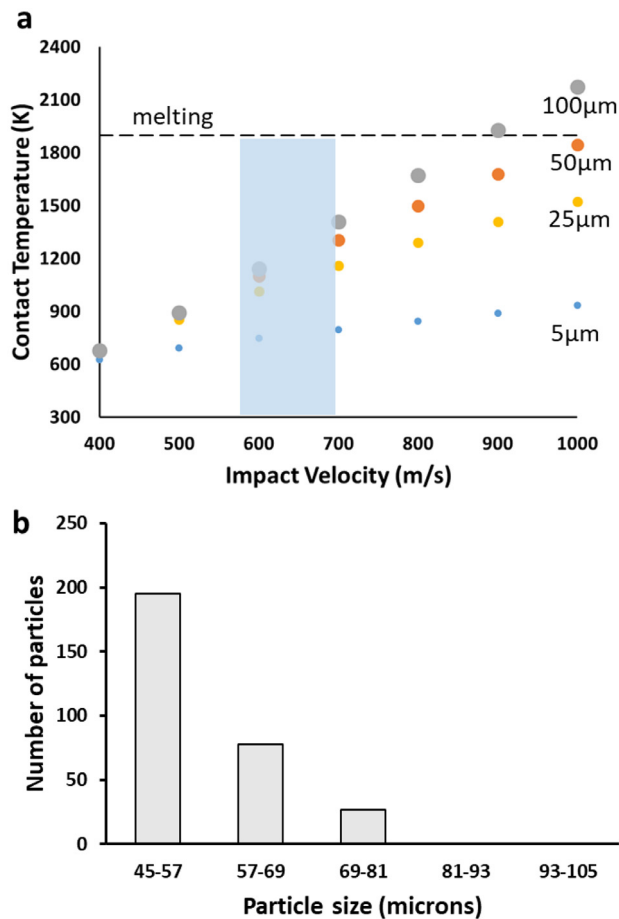


Fig. 4. (a) Contact temperature as a function of particle impact velocity and diameter, where contact temperature increases with particle size (shaded area shows the range of velocities used experimentally to fabricate porous metal deposits). (b) Particle size distribution in 3D printed porous Ti-6Al-4V (fast deposition at 800 °C).

and to increase with particle size and impact velocity for the full range of particle impact velocities (580–700 mm/s) and diameters (5–100 μm).

Analyzing the powder particle size distribution within our 3D printed porous Ti-6Al-4V deposits reveals that the majority of particles that adhered to the substrate are in a size range between 45–57 μm, and the size distribution of the deposited powder was heavily biased toward smaller particles. The original powder had a Gaussian particle size distribution with diameters between 45 and 105 μm. However, in the 3D printed porous Ti-6Al-4V deposit, 65% of the particles were in a range between 45–57 μm, 26% were between 57–69 μm, and 9% were between 69–81 μm (Fig. 4(b)). The maximum particle size in the consolidated deposit was 80 μm, whose value of η was 0.8 according to Fig. 1(c). This implies that

particles larger than 80 μm were not bonded during deposition. This finding illustrates that the effect of decreased impact velocity due to increased particle size is more significant than that of the increased contact temperature associated with larger particles. Namely, larger particles do not adhere to the surface despite their higher contact temperature because of the lower η as shown in Fig. 1(c). We note that the estimated upper particle size of 80 μm is conservative because impact induced deformation can artificially “increase” the powder size.

Scanning electron micrographs of the top view and cross section of powders after impact reveal the lateral flow of the material at all points of contact (shown by arrows in Fig. 5(a)). This is due to a localized deformation at the high impact velocity and is important in washing out the broken surface oxides from the contact zone and allowing for direct metallic bonds in addition to mechanical interlocking at the interface [15]. The cross section of a particle after impact shows an extensive grain refinement in the impact region (Fig. 5(d)) with respect to the undeformed region (Fig. 5(c)). This shows that the 3D printed constructs have spatial gradients in grain microstructure within each deposit particle due to the dynamic loading that powders experience during impact.

To determine how diffusion kinetics, especially at the interface between powder particles, influence the mechanics of 3D printed porous deposits, we performed heat treatments at 840 °C and 1050 °C for 2 h (referred to as HT840 and HT1050 in this paper). These treatments are below and above the β -transus temperature (i.e. the lowest temperature at which a 100% β phase can exist; ~970 °C for Ti-6Al-4V [32]). Porosities of the heat-treated samples are $38 \pm 4\%$ and $33 \pm 1\%$ for HT840 and HT1050, respectively. The optical micrographs of the heat-treated samples are shown in Fig. 8(a) and 8(b). The slight increase in porosity as compared to that of as-printed samples can be explained by the coalescence of small pores and/or pore rearrangement as a result of sintering [39]. X-ray diffraction measurements reveal changes in microstructure and phase structure of the material after heat treatment. Specifically, peaks in X-ray diffraction patterns become sharper after heat treatment, which corresponds to the healing of defects from deformation by recrystallization and grain growth (Fig. 6(a)). There is also a peak at $2\theta = 35.5^\circ$ after heat treatment at 1050 °C, indicating some remaining β phase after the heat treatment above the β -transus temperature. The peak intensities of α titanium indicate a slight texture of the as-deposited material, which could be attributed to the degree of deformation of particles upon impact. This texture appears more pronounced after annealing, particularly at heat treatment below β -transus temperature.

The stress-strain behavior of as-deposited porous structures under compression shows a linear regime followed by a sudden decrease in the stress-strain curve and finally a densification regime (Fig. 6(b)). At a low stress level, the deformation is homogenous throughout the specimen with an initial stress/strain ratio equal to 51.7 ± 3.2 GPa. The sample yields at 535 ± 35 MPa. Above a critical stress, a sudden drop in stress occurs that corresponds to fracture at interparticle boundaries as shown by the SEM images in Fig. 7.

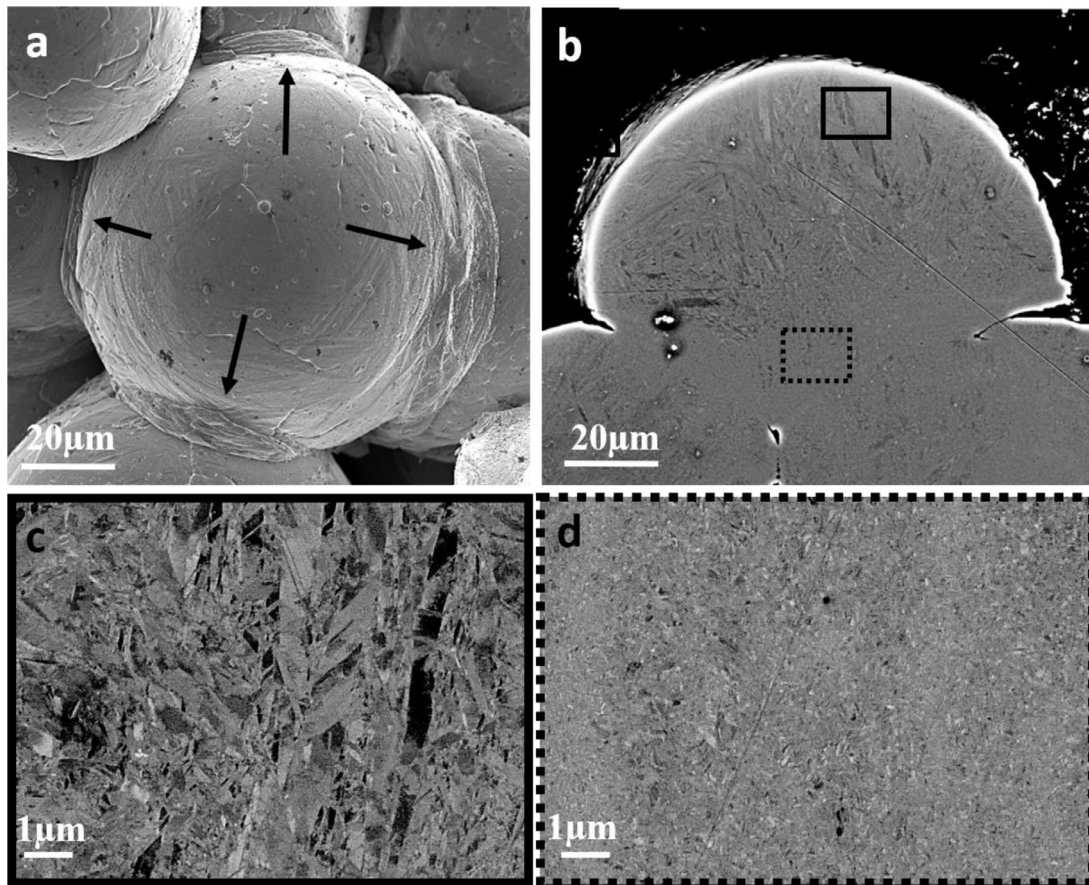


Fig. 5. Scanning electron micrographs of 3D printed Ti-6Al-4V parts. (a) Top view of a powder particle after impact. The arrows show lateral material flow at the periphery of the powder upon impact. (b) Cross section of powder after impact. (c) Magnified view of microstructure in undeformed region of powder depicted in (b). (d) Magnified view of refined microstructure at impact zone of powder depicted in (b). Frame pattern indicates the corresponding area in the cross-section overview.

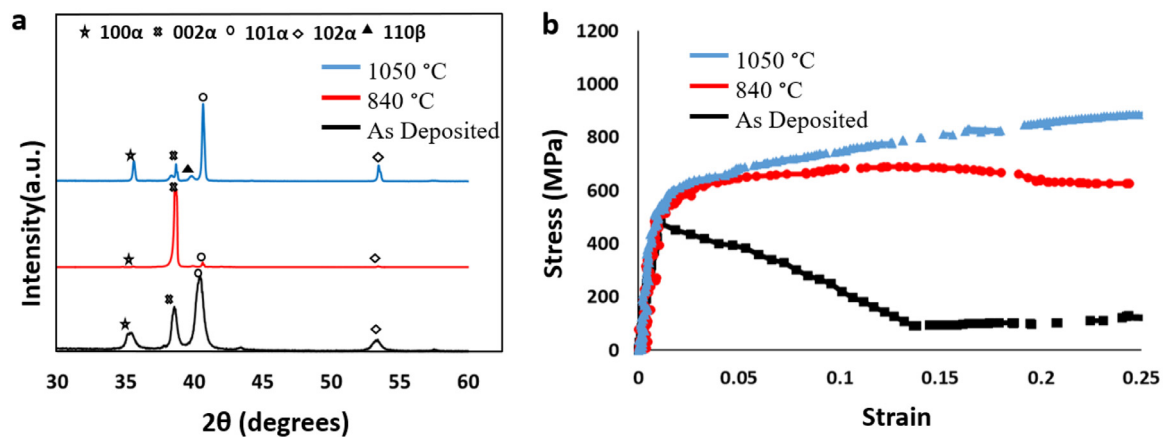


Fig. 6. Characterization of the 3D printed Ti-6Al-4V deposits in as-deposited condition and after heat treatment. (a) X-ray diffraction (XRD) pattern of as deposited and annealed samples. (b) Stress-strain behavior of as-deposited and annealed samples under compression loading.

In the heat-treated samples (HT840 and HT1050), the stress-strain behavior under compression has a linear regime, followed by a steady increase of stress as strain increases (Fig. 6(b)). The stress-strain behavior of the heat-treated sample at the elevated temperature (1050 °C) shows a higher compressive yield strength and maximum stress as compared to the heat-treated sample at a lower temperature (840 °C). The apparent initial slopes after heat treatments both above and below the β -transus temperature are comparable to that in the as-deposited sample (51.7 ± 3.2 GPa, 42.4 ± 2.6 GPa, and 55.1 ± 2.4 GPa for as-deposited, HT840, and

HT1050, respectively). However, the compressive yield stresses of both heat-treated samples are higher than that of the as-deposited (535 ± 35 MPa, 556 ± 26 MPa, and 672 ± 40 MPa for as-deposited, HT840, and HT1050, respectively). After heat treatments, the interparticle contact area may grow and become increasingly stronger due to interparticle diffusion. This can compensate for the typical softening upon coarsening of the microstructure at higher temperatures. Additionally, plastic strain up to the densification of solids is typically used to compare the behavior of different cellular solids rather than ductility according to ISO 13314. Although both as-

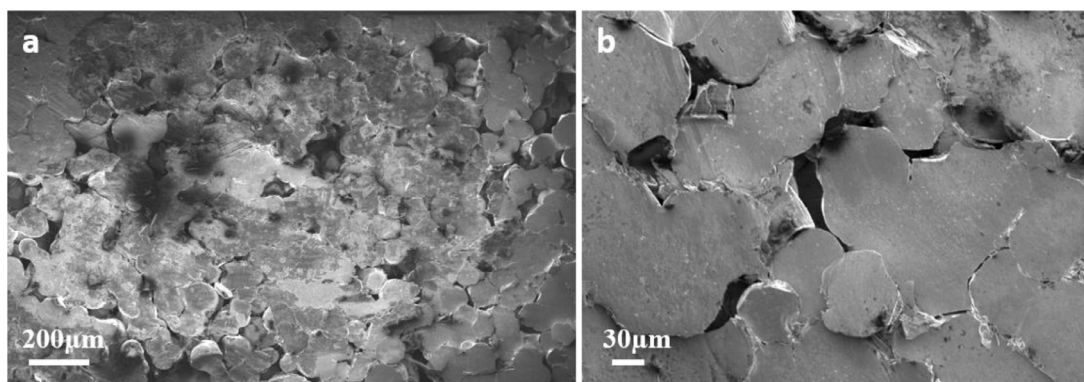


Fig. 7. Post mortem fracture analysis of as deposited samples after compression loading showing fracture at interparticle boundaries on the (a) milli scale and (b) microscale.

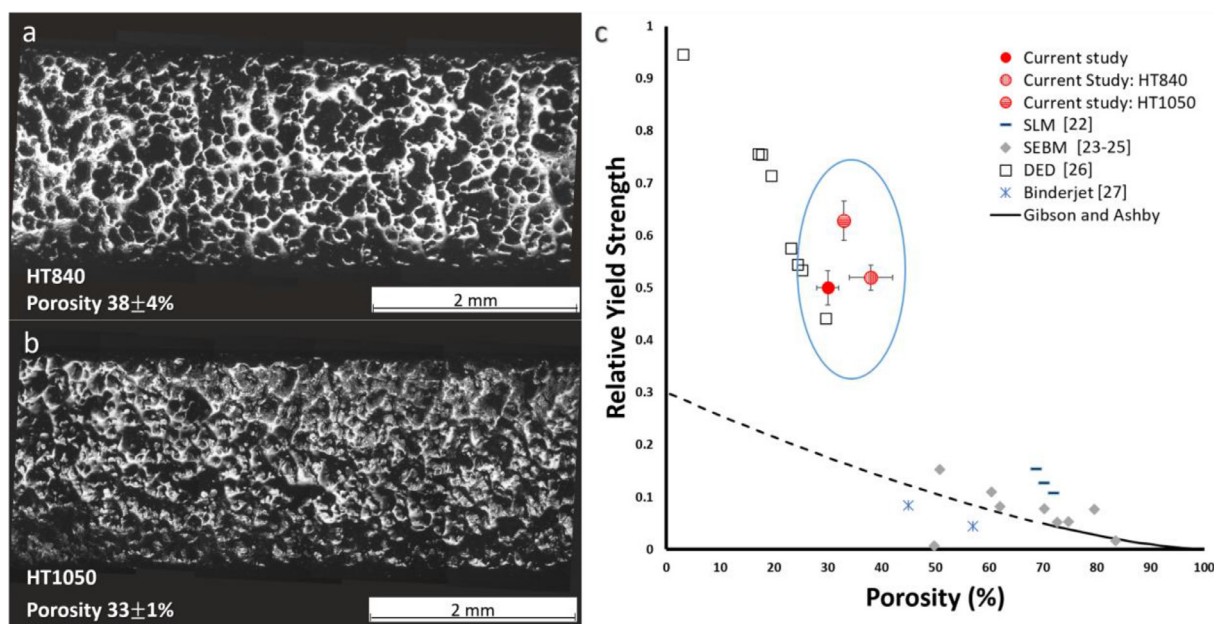


Fig. 8. Optical micrograph of cross sections of heat-treated Ti-6Al-4V porous samples at (a) 840 °C (porosity $38 \pm 4\%$) and (b) at 1050 °C (porosity $33 \pm 1\%$). (c) Relative compressive yield strength vs porosity of porous titanium structures fabricated by cold spray as well as SLM, SEBM, DED and binder jet additive manufacturing technologies. Gibson-Ashby model is plotted. The data points with similar porosity to our samples are circled in the figure.

sprayed and heat-treated samples maintain some level of structural integrity in compression, the major difference is that in as-sprayed samples, the strength drops as the strain increases. Furthermore, coarser microstructures are known to be less brittle than fine-grained material and therefore are more crack resistant. Thus, failure of contact zones becomes less likely during the deformation of annealed samples, leading to the observed steady increase in average strength until strain is increased beyond 10%. This result shows that heat treatment can serve as a new design parameter to control and improve the stress-strain behavior of porous deposits printed using cold spray, which is valuable for biomedical, structural, and energy absorption applications. Annealing conditions for designing a foam with a particular stress-strain behavior can be optimized by tuning the competing influences between stronger interparticle bonding and lower recrystallization softening for different material applications.

When compared to porous Ti-6Al-4V structures manufactured by other additive manufacturing methods such as SLM [22], SEBM [23–25], DED [26] and binder jet [27], the relative compressive yield strength values of this study are higher. Here, the relative compressive yield strength refers to the ratio of the compressive yield strength of the porous structure compared to that of a fully

dense part (1070 MPa). These values are plotted in Fig. 8(c) and listed in Table 4 (similar porosities circled in the Fig.). The expected relative compressive yield strength values from the Gibson-Ashby model are plotted for comparison. The model relates the compressive yield strength with relative density and scales with $0.3(\text{relative density})^{1.5}$, though this model only applies to porosities larger than 70% (shown by a solid line in Fig. 8(c)) [40]. Indeed, additive manufactured samples seem to follow the Gibson-Ashby model up until about 40% porosity, beyond which a large deviation from the Gibson-Ashby model occurs. This can be explained by the different deformation modes in high and low porosity ranges that result in a jump in relative compressive yield strengths; in higher porosity structures, the primary mode of deformation in compression is buckling of the cell walls, whereas in lower porosity structures, the deformation is largely shearing or yielding [40]. This shift in primary deformation mode occurs as porosity decreases because the cell walls become too stocky and short to buckle. The higher relative apparent compressive yield strength of our deposit can be attributed to significant work hardening induced by severe plastic deformation during impact, which can be a driving force for the heterogeneous recrystallization of fine grains at the impact zone after heat treatment cycles.

Table 4
Comparison of compressive yield strengths of Ti-6Al-4V porous structures.

AM	Porosity (%)	Mechanical properties Compressive yield strength (MPa)	Relative compressive yield strength	Reference
Cold Spray	30	535	0.500	Current study
	38	556	0.520	
	33	672	0.628	
SLM	70.2	136	0.127	[22]
	71.9	115	0.107	
	68.7	164	0.153	
EBM	72.7	55	0.051	[23]
	50.8	163	0.152	
	60.4	117	0.109	[24]
	70.3	83	0.078	
	49.8	7.3	0.007	[25]
	62	88	0.082	
	74.7	57	0.053	
	79.5	82	0.077	
	83.5	17	0.016	
	29.6	471.9	0.441	
25.2	571	0.534		
DED	24.4	582.6	0.545	[26]
	23	616.1	0.576	
	19.3	764.2	0.714	
	17.6	807.9	0.755	
	17	809.2	0.756	
	3	1012.7	0.946	
	17.6	807.9	0.755	
Binder jet	45	90	0.084	[27]
	57	47	0.043	

The required compressive yield strength of an implant depends on the type of the implant and the loading conditions it experiences. The yield strength of an implant could be compared with that of the bone(s) surrounding it. For example, the compressive yield strength in the human femoral cortical bone is 115 MPa [41], but a higher yield strength for implants is highly desired to avoid fracture under overloads. Generally, the yield strength of titanium alloys commonly used in biomedical implants is between 500 MPa and 1000 MPa [42]. The compressive yield stresses of the cold sprayed samples lie within this range (535 MPa, 556 MPa, and 672 MPa for as-deposited, HT840, and HT1050, respectively), making them suitable for use in implants. Moreover, a higher yield strength generally translates into higher fatigue resistance and wear resistance, both of which are important factors for implant longevity.

An additional challenge with metal implants is the mismatch in elastic modulus between the implant and the surrounding bone, which can result in stress shielding and bone resorption. Porous materials are advantageous for implants as they have lower stiffnesses than bulk materials and can reduce the harmful effects of stress shielding [46]. The elastic modulus of our material is 51.7 ± 3.2 GPa, which follows the Gibson and Ashby theory where elastic modulus scales with the relative density squared. However, the compressive yield strength of our material is 535 ± 35 MPa, which is up to 42% higher than for materials with comparable porosities manufactured by other additive manufacturing methods [26]. This margin of additional strength can be used to make a structure with higher porosity without sacrificing mechanical properties, and, thus, contribute to reducing complications due to stress shielding.

In addition to tunable mechanical properties, surface roughness, porosity, and pore size are key design parameters for biomedical implant materials, where roughness >10 μm , porosities between 30% and 50%, and pore sizes between 100 μm and 400 μm are all desirable for efficiently stimulating bone ingrowth [43,44]. To evaluate the suitability of porous Ti-6Al-4V for biomedical applications, surface roughness, contact angle measurement, and biocompatibility studies are performed. The arithmetic mean surface roughness of our 3D printed titanium alloy is 37 μm , which is

Table 5

Surface roughness parameters of bulk titanium substrates and 3D printed Ti-6Al-4V deposits. * Parameters are according to ISO 4278 geometrical product specification. S_a : Arithmetic average, S_q : Root mean square, S_v : Maximum valley depth, S_p : Maximum peak height

Treatment	$S_a(\mu\text{m})^*$	$S_q(\mu\text{m})$	$S_v(\mu\text{m})$	$S_p(\mu\text{m})$
Substrate	6	8	54	68
T800-Fast	37	47	231	204
T900-Fast	36	46	209	212

more than six times the surface roughness of the as-received substrate. The surface roughness falls into the macro roughness regime (roughness >10 μm), which is important for long-term mechanical stability and biomedical applications related to primary bone implant fixation [44]. Roughness parameters (arithmetic average, root mean square, maximum valley depth, and maximum peak height) are tabulated in Table 5. Contact angle measurement against distilled water is not possible on these samples, as the droplet is absorbed instantaneously into the pores of the surface (Supplemental Movie S1). This confirms the open-cell structure of the 3D printed titanium alloy. Open cell structures are particularly important for biomedical applications of porous materials as they allow for the transport of nutrients, oxygen, and waste products to and from cells adhering to the porous substrates.

Murine preosteoblast cells (MC3T3-E1 SC4, $P < 7$) are found to be biocompatible with cold spray fabricated porous Ti-6Al-4V deposits. Preosteoblast cells adhere to the surface of the porous Ti-6Al-4V and maintain viability over the course of seven days as demonstrated by predominantly live cells and a few dead cells being present after seven days of growth (Fig. 9(a-c)). The porous nature of the 3D architecture of the deposit allowed cells to integrate into the first 275 ± 12 μm of the porous Ti-6Al-4V, as shown in Fig. 9(d). Cells grew directly on the surface of the particles as well as between them as evidenced by confocal microscopy (Fig. 9(e)) and corroborated by SEM imaging (Fig. 9(f,g)). Pores at the surface have sizes in the range of 80 to 320 μm , which is within the size range shown to be optimal for bone ingrowth (50 to 800 μm) [17]. These biocompatibility experiments demonstrate that pre-osteoblasts are capable of integrating into

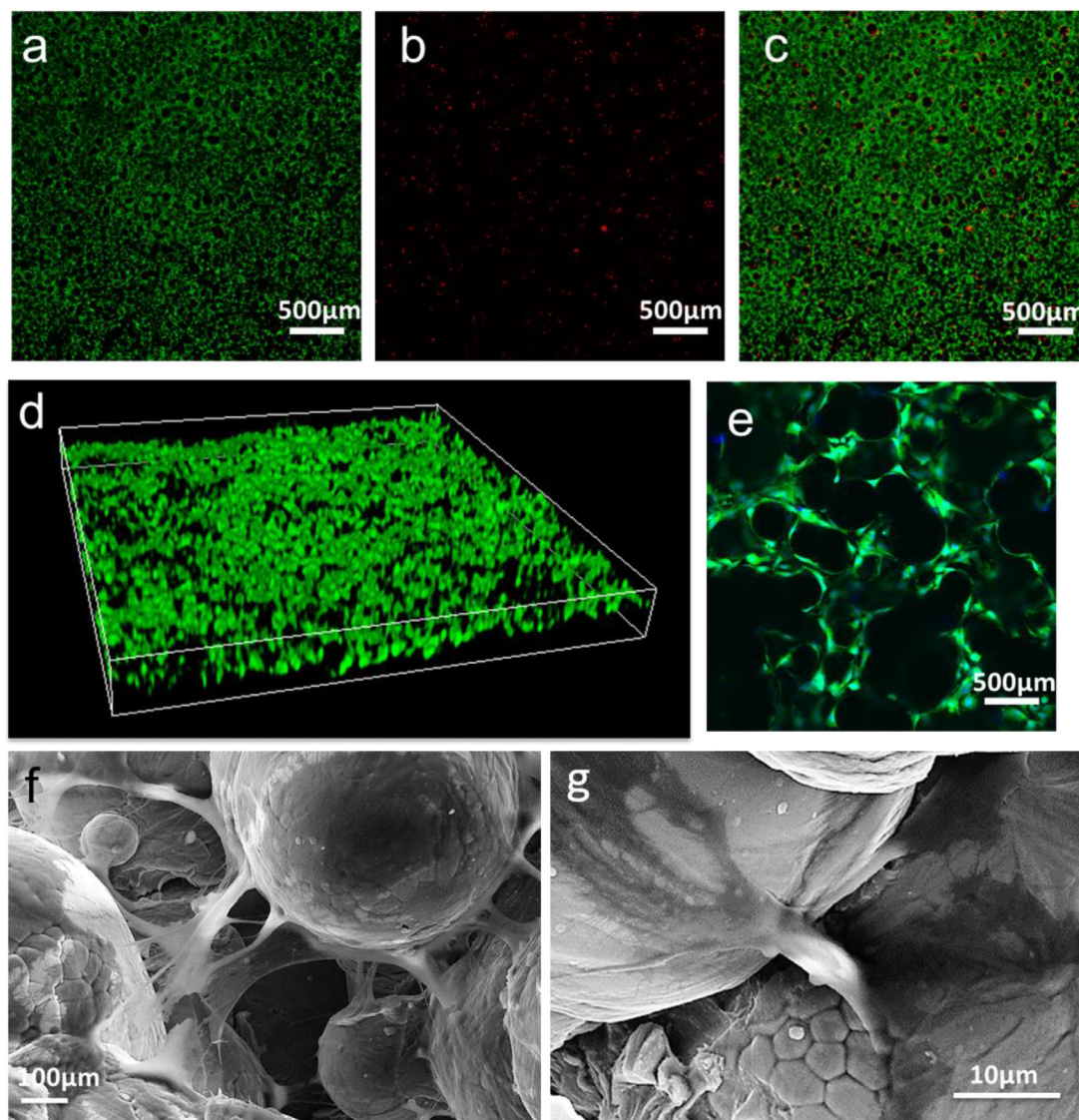


Fig. 9. Biocompatibility of murine preosteoblasts with Ti-6Al-4V metallic foam. (a-c) Representative LIVE (green, a)/DEAD (red, b) and merged (c) confocal microscopy images of cells that grew within the first 275 μm of a porous titanium substrate. Images are projection images of the average intensities from confocal microscopy image volumes of 3.2 mm x 3.2 mm x 275 μm . (d) Rendering of a 3D image volume of preosteoblasts that grew 275 μm into the Ti-6Al-4V porous deposit. (e) Murine preosteoblasts (live cells- green, cell nuclei-blue) growing around and between titanium powder. Ti-6Al-4V particles are the spherical black voids within the image. (f) SEM images of cells on surfaces of 3D printed Ti-6Al-4V powders. (g) Magnified view of cells on 3D printed porous titanium. (For interpretation of the references to colour in this figure legend, the reader is referred to the web version of this article.)

the interstices of the pores of the cold spray fabricated titanium alloy while maintaining their viability, which reveals the utility of these materials for cellular ingrowth – an essential characteristic of successful bone scaffolds [45].

Beyond biomedical applications, the one-step nature of the process and the high deposition rates of cold spray (10 cm^3/min as opposed to 10 cm^3/hour in powder bed metal additive manufacturing [17,47]) make the method attractive for the fabrication of cellular metals with large-scale industrial applications in construction, transportation, and energy. Additionally, the one-step subcritical cold spray deposition can be adopted to deposit cellular structures using a wide range of metallic materials that are already in use in cold spray processing. In this work, we printed simple rectangular geometries to understand the deposition kinetics and mechanical properties of these structures. However, this can be easily adopted to make 3D objects by integrating the supersonic nozzle in cold spray with a commercially available robot as is already achieved by companies such as Impact Innovations [48], NRC Canada [49] and Speed3D [50].

4. Conclusion

Subcritical cold spray is demonstrated to enable one-step fabrication of porous Ti-6Al-4V structures printed by accelerating powders to supersonic impact velocities. Nozzle traverse speed is tuned to control the distribution of porosity across the deposit thickness. With specific deposition parameters ($V_N = 12$ m/min, $\eta \sim 0.8$, $P = 40$ bar, $T = 800$ °C), a uniform porosity of $30 \pm 2\%$ is obtained. The density of the deposit is demonstrated to be a function of nozzle traverse speed and normalized powder impact velocity (η). The apparent Young's modulus of the 3D printed titanium alloy (51.7 ± 3.2 GPa) follows the Gibson and Ashby theory while the compressive yield strength (535 ± 35 MPa) is up to 42% higher than those of the porous structures manufactured by other additive manufacturing methods with comparable porosities. After heat treatment, the elastic modulus does not change significantly, but the average strength shows a steady increase until plastic strain is increased beyond 10%. Finally, the printed porous metal deposits prove as biocompatible, demonstrating the utility of 3D solid-state

cold spray printing as a potential manufacturing method for producing biomedical implant materials.

Declaration of Competing Interest

The authors declare no competing financial interests.

Acknowledgement

A.M., M.G. and M.D. acknowledge the financial support from MIT-Italy global seed fund. A.M., M.G. acknowledge the financial support from Polimi International Fellowship.

Author information

Correspondence and requests for materials should be addressed to A.M. (moridi@cornell.edu) or M.D. (mingdao@mit.edu).

Author contributions

A.M., F.G., H.A. and M.D. conceived the ideas and designed the project. M.D., T.K, M.G, and A.M. supervised the project, A.M. and A.W. performed mechanical characterizations. A.M. and E.J.S. designed and conducted biocompatibility studies. A.M., E.J.S. and M.D. wrote the manuscript with input from all authors.

Data availability

Data supporting the findings of this study are available in the main text and supplementary information. Additional information is available upon reasonable request.

Supplementary materials

Supplementary material associated with this article can be found, in the online version, at doi:10.1016/j.apmt.2020.100865.

References

- [1] M.F. Ashby, et al., Metal foams : a design guide metal foams : a design guide, Library 54 (2000).
- [2] J. Banhart, Manufacturing routes for metallic foams, Jom 52 (2000) 22–27.
- [3] H.N.G. Wadley, Cellular metals manufacturing, Adv. Eng. Mater 4 (2002) 726–733.
- [4] D.J. Sypeck, H.N.G. Wadley, Cellular metal truss core sandwich structures, Adv. Eng. Mater 4 (2002) 759–764.
- [5] A.G. Evans, J.W. Hutchinson, N.a. Fleck, M.F. Ashby, H.N.G. Wadley, The topological design of multifunctional cellular metals, Prog. Mater. Sci. 46 (2001) 309–327.
- [6] C.B. Williams, J.K. Cochran, D.W. Rosen, Additive manufacturing of metallic cellular materials via three-dimensional printing, Int. J. Adv. Manuf. Technol. 53 (2011) 231–239.
- [7] P. Newman, H. Zreiqat, Design and fabrication of 3D printed scaffolds with a mechanical strength comparable to cortical bone to repair large bone defects, Sci. Rep. (2016) 1–8.
- [8] W.J. Sames, F.A. List, S. Pannala, R.R. Dehoff, S.S. Babu, The metallurgy and processing science of metal additive manufacturing, Int. Mater. Rev. 61 (2016) 315–360.
- [9] Y.M. Wang, et al., Additively manufactured hierarchical stainless steels with high strength and ductility, Nat. Mater. (2018), doi:10.1038/NMAT5021.
- [10] J.H. Martin, et al., 3D printing of high-strength aluminium alloys, Nature 549 (2017) 365–369.
- [11] D.C. Hofmann, et al., Developing gradient metal alloys through radial deposition additive manufacturing, Sci. Rep. 4 (2014) 5357.
- [12] W.E. Frazier, Metal additive manufacturing: a review, J. Mater. Eng. Perform 23 (2014) 1917–1928.
- [13] B. Vayre, F. Vignat, F. Villeneuve, Metallic additive manufacturing: state-of-the-art review and prospects, Mech. Ind. 13 (2012) 89–96.
- [14] A Moridi, Powder Consolidation Using Cold Spray: Process Modeling and Emerging Applications, Springer Briefs in Applied Sciences and Technology, 2016.
- [15] A. Moridi, S.M. Hassani-Gangaraj, M. Guagliano, M. Dao, Cold spray coating: review of material systems and future perspectives, Surf. Eng. 30 (2014) 369–395.
- [16] H. Assadi, F. Gärtner, T. Stoltenhoff, H. Kreye, Bonding mechanism in cold gas spraying, Acta Mater 51 (2003) 4379–4394.
- [17] X.P. Tan, Y.J. Tan, C.S.L. Chow, S.B. Tor, W.Y. Yeong, Metallic powder-bed based 3D printing of cellular scaffolds for orthopaedic implants: a state-of-the-art review on manufacturing, topological design, mechanical properties and biocompatibility, Mater. Sci. Eng. C 76 (2016) 1328–1343.
- [18] A. Moridi, et al., Deformation and failure mechanisms of Ti – 6Al – 4V as built by selective laser melting, Mater. Sci. Eng. A 768 (2019) 138456.
- [19] A. Dass, A. Moridi, State of the art in directed energy deposition: from additive manufacturing to materials design, Coatings 9 (2019) 418.
- [20] S. Liu, Y. Zhang, R. Kovacevic, Numerical simulation and experimental study of powder flow distribution in high power direct diode laser cladding process, Lasers Manuf. Mater. Process. 2 (2015) 199–218.
- [21] J. Kim, A. Wakai, A. Moridi, Materials and manufacturing renaissance : additive manufacturing of high-entropy alloys. 1, (2020).
- [22] J. Wieding, A. Jonitz, R. Bader, The effect of structural design on mechanical properties and cellular response of additive manufactured titanium scaffolds, Materials (Basel) 5 (2012) 1336–1347.
- [23] Y.J. Liu, et al., Compressive and fatigue behavior of beta-type titanium porous structures fabricated by electron beam melting, Acta Mater 126 (2017) 58–66.
- [24] J. Parthasarathy, B. Starly, S. Raman, A. Christensen, Mechanical evaluation of porous titanium (Ti6Al4V) structures with electron beam melting (EBM), J. Mech. Behav. Biomed. Mater. 3 (2010) 249–259.
- [25] S.J. Li, et al., Compression fatigue behavior of Ti-6Al-4V mesh arrays fabricated by electron beam melting, Acta Mater 60 (2012) 793–802.
- [26] A. Bandyopadhyay, et al., Influence of porosity on mechanical properties and in vivo response of Ti6Al4V implants, Acta Biomater 6 (2010) 1640–1648.
- [27] S. Barui, S. Chatterjee, S. Mandal, A. Kumar, B. Basu, Microstructure and compression properties of 3D powder printed Ti-6Al-4V scaffolds with designed porosity: experimental and computational analysis, Mater. Sci. Eng. C 70 (2017) 812–823.
- [28] T. Schmidt, et al., From particle acceleration to impact and bonding in cold spraying, J. Therm. Spray Technol. 18 (2009) 794–808.
- [29] H. Assadi, et al., On parameter selection in cold spraying, J. Therm. Spray Technol. 20 (2011) 1161–1176.
- [30] available in the software from kinetic-spray-solutions.com, Buchholz, Germany.
- [31] K. Binder, Kaltgasspritzen von ermüdungsfesten Titanschichten, Helmut-Schmidt-Universität, 2013.
- [32] Y.V.R.K., Prasad, T. Seshacharyulu, Processing maps for hot working of titanium alloys. 243, 82–88 (1998).
- [33] Ed., 1st. ISO 4278. Geometrical product specifications (GPS) – surface texture: profile method- terms, definitions and surface texture parameters. (1997).
- [34] A.R. Robson, P. Basu, Equations of Mathematical Physics, The Macmillan Company, 1963.
- [35] A. Papyrin, V. Kosarev, S. Klinkov, A. Alkhimov, V.M. Fomin, Cold Spray Technology. (2007).
- [36] W.-S. Lee, C.-F. Lin, High-temperature deformation behaviour of Ti6Al4V alloy evaluated by high strain-rate compression tests, J. Mater. Process. Technol. 75 (1998) 127–136.
- [37] Z. Arabgol, M. Villa Vidaller, H. Assadi, F. Gärtner, T. Klassen, Influence of thermal properties and temperature of substrate on the quality of cold-sprayed deposits, Acta Mater 127 (2017) 287–301.
- [38] A.W.Y. Tan, et al., Effects of traverse scanning speed of spray nozzle on the microstructure and mechanical properties of cold-sprayed Ti6Al4V coatings, J. Therm. Spray Technol. 26 (2017) 1484–1497.
- [39] J. Ekberg, A. Ganvir, U. Klement, S. Creci, L. Nordstierna, The influence of heat treatments on the porosity of suspension plasma-sprayed yttria-stabilized zirconia coatings, J. Therm. Spray Technol. 27 (2018) 391–401.
- [40] L.J. Gibson, M. Ashby, Cellular Solids, Structure and Properties, Cambridge university press, 1997, doi:10.1557/mrs2003.79.
- [41] E.F. Morgan, G.U. Unnikrisnan, A.I. Hussein, Bone mechanical properties in healthy and diseased states, Annu. Rev. Biomed. Eng. 20 (2018) 119–143.
- [42] N. Mitsuo, Mechanical properties of biomedical titanium alloys, Mater. Sci. Eng. A 243 (1998) 231–236.
- [43] K. Palka, R. Pokrowiecki, Porous titanium implants: a review. (2018).
- [44] M.M. Shalabi, A. Gortemaker, M.A.V. Hof, J.A. Jansen, N.H.J. Creugers, Implant surface roughness and bone healing: a systematic review, J. Dental Res. 85 (2006) 496–500.
- [45] X. Wang, et al., Topological design and additive manufacturing of porous metals for bone scaffolds and orthopaedic implants: a review, Biomaterials 83 (2016) 127–141.
- [46] S. Bhattacharya, J. Bustillos, F.Q. Gonzalez, J.A. Spector, A. Moridi, Biomedical applications of metal additive manufacturing: current state-of-the-art and future perspective, Am. J. Biomed. Sci. Res. 7 (2020) 6–10.
- [47] J Villafuerte, Modern Cold Spray, Springer, 2015.
- [48] https://www.impact-innovations.com/en/coldgas/cg_index_en.html.
- [49] https://nrc.canada.ca/en/research-development/research-collaboration/industrial-rd-groups/cold-spray-additive-manufacturing-csam-industrial-rd-group.
- [50] https://www.spee3d.com/.

Solid-State Additive Manufacturing of Porous Ti-6Al-4V by Supersonic Impact

Atieh Moridi^{1,2,3*}, Elizabeth J. Stewart^{1,4}, Akane Wakai², Hamid Assadi⁵, Frank Gartner⁶,
Mario Guagliano³, Thomas Klassen⁶, Ming Dao^{1*}

¹ Department of Materials Science and Engineering, Massachusetts Institute of Technology, Cambridge, MA, 02138, USA. ² Sibley School of Mechanical and Aerospace Engineering, Cornell University, Ithaca, NY, 14853, USA. ³ Department of Mechanical Engineering, Polytechnic University of Milan, Milan, Italy. ⁴ Department of Chemical Engineering, Worcester Polytechnic Institute, Worcester, MA, 01609, USA. ⁵ Brunel University London, Brunel Centre for Advanced Solidification Technology (BCAST), Uxbridge, United Kingdom. ⁶ Helmut Schmidt University, University of the Federal Armed Forces, Hamburg, Germany.

*Corresponding author: moridi@cornell.edu or mingdao@mit.edu

Supplementary Materials

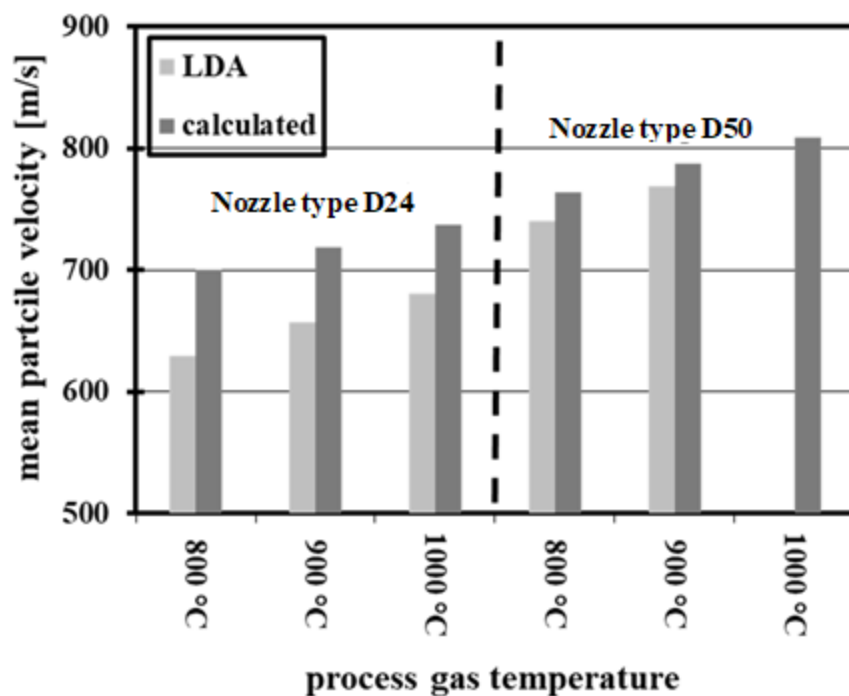


Figure S1: Comparison of experimentally determined and calculated particle velocities for cold spraying of pure titanium, as obtained from LDA and isentropic simulations using a development version of KSS-software, respectively. For covering a rather wide range of conditions, nozzles with throat diameters of 2.7 mm (D24) and 3.8 mm (D50), as well as different process gas temperatures were used. The process gas pressure was kept fixed at $P_{\text{gas}} = 4$ MPa. The velocities were determined at a stand-off distance of 60 mm. The calculations were performed for spherical particles with sizes of 45 μm . This figure has been redrawn from Figure 5.10 in Ref. 31 (Binder, K. Kaltgassspritzen von ermüdungsfesten Titanschichten. (Helmut-Schmidt-Universität, 2013).) Note that these verification experiments have also been used as a basis for introducing correction functions into the officially released version of KSS software (used in this study) so that calculations using KSS software closely match experimental values.

Movie S1: A droplet of distilled water is absorbed instantaneously into the pores of the surface of a 3D-printed porous Ti-6Al-4V sample.